Strain field measurements around notches using SIFT features and meshless methods

GIANCARLO GONZÁLES* AND MARCO MEGGIOLARO

Department of Mechanical Engineering, PUC-Rio, Rua Marquês de São Vicente 225, Gávea, Rio de Janeiro, RJ—22543-900 Brazil
*Corresponding author: giancarlo.g.gonzales@outlook.com

This work proposes a hybrid experimental-numerical technique with the aim to improve strain measurements at stress concentration regions. The novel technique is performed employing the computer vision scale invariant feature transform (SIFT) algorithm and meshless methods, here termed SIFT-meshless. The SIFT is applied to perform feature points matching in two images of the specimen surface at different stages of mechanical deformation. The output data are provided as a set of displacement measurements by tracking matched feature points. This information is then used to model displacement and strain field on the surface by means of a meshless formulation based on the moving least squares approximation. By applying the proposed SIFT-meshless method, the strain distribution around a semicircular notch in a plate under bending load was investigated. The experimental results were compared with those obtained by a digital image correlation technique based on a subset approach and to simulations from finite element analysis software. The experimental results demonstrated that the present method is capable of performing reliable strain measurements at distances close to the notch where the peak strain value is expected, even in the presence of high strain gradients. © 2015 Optical Society of America

1. INTRODUCTION

Stress analysis is important for the safe design and manufacture of mechanical components and structural elements. Theoretical analysis uses the classical strength of materials equations, which are only valid in regions of the component where no geometric irregularities have occurred. However, it is difficult to design a machine avoiding changes in geometry of the members. Most mechanical components contain holes, grooves, keyways, and shoulders, generally termed notches. During operation, these changes in geometry increase significantly the local stress and strain levels, which may be several times larger than the nominal values calculated for the section [1]. The stress concentration caused by the presence of notches is important in many failure mechanisms, such as fatigue crack initiation. Consequently, there is a real need for tools that can deal with nontrivial geometric shapes under different load conditions.

In past years, experimental mechanics investigations has attracted increasing attention due to their ability to provide information of the mechanical solicitations through measurements made directly on the specimen surface. Traditionally, the strain gage is by far the most popular device for measuring mechanical solicitations in terms of strains. In general, the strain gauge is to be used to measure the strain at the center of the gauge. However, the magnitude of the error in strain

gauge measurements is dependent on the gauge dimensions and position. Thus, the accuracy of the strain gauge is affected when it is placed near a stress concentration region where the strain gradient is high (i.e., there is a large change in strain values within a small distance). This is due to the fact that the gauge is of finite length and it inherently underestimates the maximum strain at the notch root [2].

On the other hand, optical techniques have distinct advantages of being noncontact, nonintrusive, and full-field measurement techniques. Furthermore, these techniques have greatly benefited from the technological advances in image acquisition and processing. Among the main optical techniques, digital image correlation (DIC) [3–5] is nowadays the most used in experimental mechanics due to its simplicity and versatility.

DIC techniques involve a process of subset-based matching in which two images from a properly prepared specimen are required: a reference image (unloaded stage of the specimen) and deformed image (respective loaded stage of the specimen). First, the reference image is divided into small subsets, and then the algorithm attempts to find the same pattern of pixel intensities on the second image using a correlation criterion. By tracking the positions of subsets between the reference image and the deformed image, the full-field displacement on the surface is obtained, and the resulting strains can be derived.

DIC has been improved since its invention in the early 1980s; many applications of this technique can be found in the literature for the determination of strain fields under different loading conditions [6–9], including those around notches [10–12]. However, reliable measurement values in the presence of high strain gradients near the edge of the notches may present some challenges to DIC techniques. It is known that the measured gradients are always more flattened than the real ones; this is because the required subset for the analysis has a necessarily finite dimension. Therefore, the choice of the subset size is considered critical to the accuracy of the measured displacements [13,14]. If a too small subset is utilized, the pixel information may not be sufficient to be discriminated from the other subsets. In contrast, a too large subset may mask nonhomogeneous strain fields. The user must rely on experience and intuition to manually define a proper subset size to achieve a reliable solution.

In this study, a different approach to the classical subset-based matching is used for image correlation by applying feature-based matching. Features are pieces of information that are selected for having significant attributes, and they can be useful for constructing local descriptors with robust properties. Thus, the feature points in the reference and deformed images can then be matched by comparing their descriptors.

Currently, the most well-known feature descriptor is the scale invariant feature transform (SIFT) originally proposed by Lowe [15] and improved later on in [16]. According to Lowe, this technique transforms an image into a large collection of local feature vectors, each of which is invariant to image translation, scaling, and rotation and partially invariant to illumination changes and affine or 3D projection.

The SIFT technique is widely used in several computer vision applications due to its robustness and distinctiveness in image matching tasks, as indicated in [17,18].

This study proposes a novel method for full-field strain measurements using the advantages of SIFT descriptors for automating the image correlation process. First, the SIFT algorithm is used to match homologous points in the undeformed/deformed pair of images. Then, the tracking of successful matches allows the experimental determination of the displacement field on the specimen surface. Finally, these SIFT points are used in a meshless formulation to model the displacement field and its derivatives.

In the last decades, meshless methods have been considerably improved [19–21]. These numerical methods are mainly characterized by not requiring a mesh to represent the problem domain, depending exclusively on a set of nodes scattered within it. This flexibility allows the SIFT key points to be used as nodes in the meshless formulation. In this study, the moving least squares (MLS) method is adopted for the construction of shape functions used for the approximations. This procedure is similar to the element-free Galerkin method proposed by Belytschko co-worker [22,23].

The meshless formulation was performed to improve accuracy of the approximate solutions, particularly in the proximity of notches or geometric discontinuities. A strain gradient indicator, based on the evaluation of the first approximation solution, is used to automatically update the parameters of the formulation when a strain concentration region is localized, in which higher accuracy is required.

In order to validate the present method, the deformation behavior in the region of stress concentration of a 304 stainless-steel plate with a semicircular notch is investigated. For that, a four-point bending test is carried out on the specimen. The obtained results are compared to analyzes using the commercial software VIC-3D developed by correlated solutions [24], and to finite element (FE) simulations using the commercial code ANSYS. Finally, the performance of the proposed method for strain measurement around notches is discussed.

2. PROPOSED SIFT-MESHLESS METHOD

The proposed SIFT-meshless method is divided into two main steps. The first one consists in the experimental determination of displacements using the SIFT technique, and the second involves applying the meshless approximations to solve the displacement and strain fields.

A. Displacement Measurements by SIFT

The SIFT technique is used here to measure the displacements of homologous feature points successfully matched by processing two images from a specimen captured before and after deformation (see Fig. 1). In this work, an implementation of Lowe's SIFT is used, which is publicly available via [25].

The tracking feature procedure based on the SIFT algorithm involves three steps: feature detection, feature description, and feature matching. The procedures of SIFT are briefly described here, and more details about the algorithm can be found in [16].

1. Feature Detection

In the feature detection step, potential feature points are detected by searching over all scales and image locations. This can be implemented efficiently by constructing a Gaussian pyramid and searching for local peaks (maxima or minima) in a series of difference of Gaussian (DoG):

$$D(x, y, \sigma) = [G(x, y, k\sigma) - G(x, y, \sigma)] * I(x, y), \quad \textbf{(1)}$$

where $G(x, y, \sigma)$ is variable scale Gaussian, $I(x, y)$ is the input image, and $*$ is the convolution operation in x and y of the $G(x, y, \sigma)$. DoG scale space is computed from the difference of two nearby scales separated by constant multiplicative factor k.
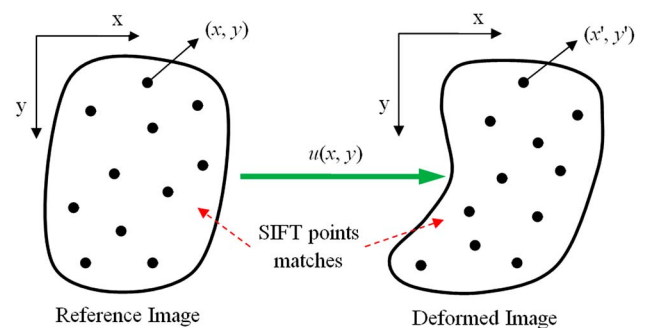

Fig. 1. Displacement measurements by matching SIFT features.

SIFT guarantees that the feature points, called key points, are located at regions and scales of high variations, which make these locations stable for characterizing the image.

Once key point candidates have been found, their location and scale can be determined accurately by fitting a 3D quadratic function around each key point (reaching the subpixel accuracy). This approach uses the Taylor expansion up to the quadratic terms of the scale space function $D(x, y, \sigma)$:

$$D(\mathbf{x}) = D + \frac{\partial D}{\partial \mathbf{x}}\mathbf{x} + \frac{1}{2}\mathbf{x}^T \frac{\partial^2 D}{\partial \mathbf{x}^2}\mathbf{x}, \qquad (2)$$

where D and its derivatives are evaluated at the sample point and $\mathbf{x} = (x, y)^T$ is the offset from this point. The location of the local peak, $\mathbf{x}'$, is determined by taking the derivative of this function with respect to $\mathbf{x}$ and setting it to zero, giving

$$\mathbf{x}' = -\frac{\partial^2 D^{-1}}{\partial \mathbf{x}^2}\frac{\partial D}{\partial \mathbf{x}}. \qquad (3)$$

The final key points are selected based on measures of their stability; low contrast points (sensitive to noise) and points along edges (hardly be distinguished from each other) are removed.

2. Feature Description

In the feature description step, a local descriptor for each feature point is computed.

First, a consistent orientation is assigned to the key points based on local image gradient directions. In other words, for every pixel in the neighborhood of the key points, the intensity gradient (magnitude and orientation) is computed. An orientation histogram is established by the weighted gradient magnitudes: the highest orientation histogram peak represents the principal direction of the feature points, while the peaks with amplitudes greater than 80% of the highest peak are used to create an additional key point with the corresponding orientation. Moreover, a parabola is fit to interpolate the peaks' position in order to reach more accurate orientation assignment.

Last, a local image descriptor for each key point is constructed based on the magnitudes and orientations of the image gradients in the neighborhood of the key point. Each region is rotated based on its dominant orientation and partitioned into 16 subregions of 4×4 pixels. For each pixel within a subregion, SIFT accumulates the pixel's gradient to orientation histograms with eight bins by weighting the contribution of each gradient according to its magnitude, which forms a 128-element vector. To reduce the effects of changes in illumination, this vector is normalized to unit length. Thus, the 128-element vector constructs the feature descriptor, as shown in Fig 2.

3. Feature Matching

The feature-matching step is to find the feature correspondences between successive images by comparing their descriptors. Commonly, the Euclidean distance is the most used metric to measure similarity between descriptors. The matches are identified by finding the closest descriptor (minimum Euclidean distance) of each key point from the first image (reference image) among those in the second image (deformed image).

In order to discard poorly or too ambiguous matched features, a subsequent threshold is used. If the distance ratio between the closest descriptor and the second-closest descriptor is
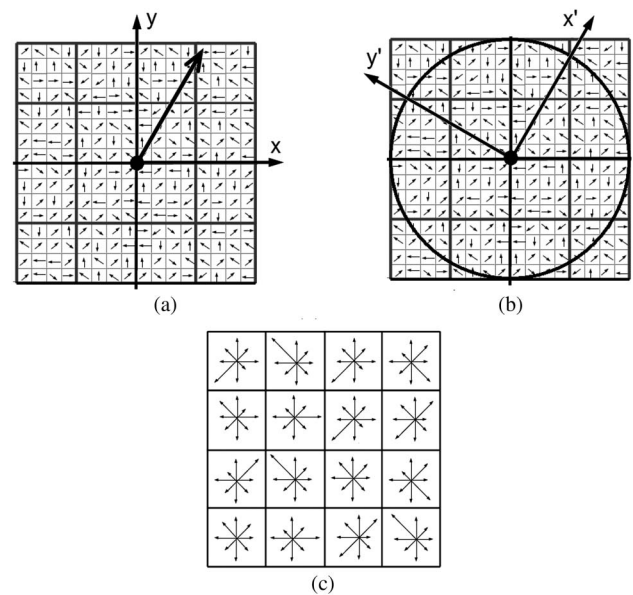

Fig. 2. Descriptor construction. (a) Computation of the magnitude and orientation around the key point for orientation assignment. (b) Orientation corrections and spatial coordinate transformation. (c) SIFT descriptor establishment.

below a certain threshold, then the match is kept; otherwise, the match is rejected and the feature is removed. In common SIFT applications, a distance ratio between 0.6 and 0.8 is used, as recommended by Lowe. In the present experimentation, the threshold is adjusted down to select only the most reliable, according to [16] (see key point matching). From experimental results conducted by the authors, a distance ratio of 0.3–0.4 is found to lead to good matching results.

Thus, by using the SIFT algorithm, it is possible to detect stable feature points from a single image, even though not all of them are useful. To maximize the number of possible interest points that can be detected by SIFT, an appropriate random pattern on the specimen surface is required. Since the specimen surface originally does not show a suitable texture, a similar strategy to that used in DIC techniques can be applied. A typical random speckle pattern is created by spraying a uniform white paint layer as a base, and then black random dots are inserted, as shown in Fig. 3(a). As a result, a large number of SIFT features can be extracted from this region, which are plotted in Fig. 3(b). They also can be used to perform reliable matching between images with different views of a same object, as shown in Fig. 3(c).

Moreover, since a stereovision system is used to capture the images, stereo calibration has to be performed before the experiment. This procedure refers to the determination of camera parameters, which are used to model the imaging process and the location of the cameras in its environment. The quality of the stereo calibration is an important factor that determines accuracy of the optical measurement system. For the correspondence problem, the SIFT technique is also used to determine matches in the left and right camera images. Finally, the information of calibration and correspondence step are used to recover the 3D position from the 2D image point pair based on a stereo triangulation algorithm.

(a)   (b)

(c)
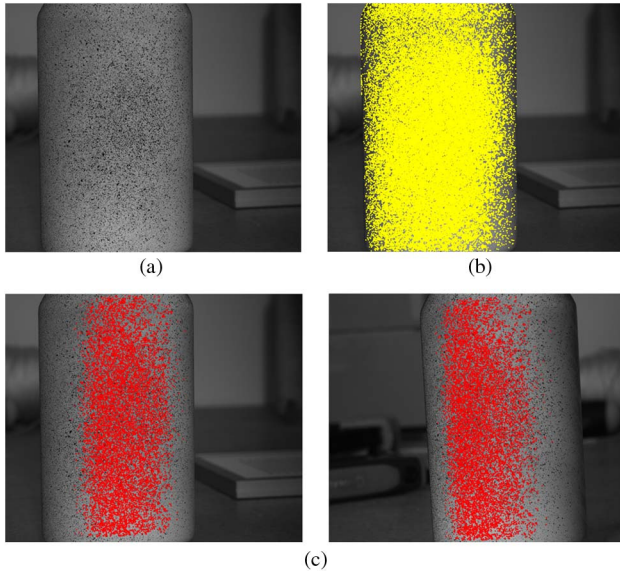
Fig. 3. (a) Image of an object with contrasting pattern on the surface. (b) SIFT features detected from the original image. (c) Example of typical matching result using an object with viewpoint change.

B. Meshless Formulation

Once the SIFT features are located in an undeformed/deformed pair of images, they are selected as field nodes in a meshless formulation. Thus, the u component of the displacement field at an arbitrary point $\mathbf{x}^T = [x, y]$ in the problem domain is approximated using the nodal displacements within a local domain or small neighborhood around the point $\mathbf{x}$. Mathematically,

$$u(\mathbf{x}) = \sum_{i}^{n} \phi_i(\mathbf{x}) u_i, \qquad (4)$$

where n is the number of nodes in the local domain of $\mathbf{x}$, $\phi_i(\mathbf{x})$ is the shape function of the i-th node, and u_i represents the nodal displacements provided by tracking SIFT features.

The shape functions are locally supported because only a determined set of field nodes around point $\mathbf{x}$ is used to support or approximate the function value at $\mathbf{x}$. For domains with irregularly distributed nodes (as shown by the SIFT features in Fig. 3), the use of an influence domain works well to select nodes for approximations. The influence domain represents the region where a node exerts its influence, and it is defined for each node in the problem domain, as shown in Fig. 4. It can be seen that the influence domain never extends outside the problem domain. In case of discontinuities, it is limited to those neighbor points, which can be connected to the point of interest without intersecting a boundary of the problem domain. The shapes most often used are circular or rectangular. In this work, the circular shape is adopted.

In Fig. 4, the node termed $\mathbf{x}$ is within the influence domain of nodes 1 and 2. Later, these nodes will be used to construct the shape function for point $\mathbf{x}$. Node 3 will not be used because it does not have any influence on point $\mathbf{x}$.

The dimension of the influence domain determines the number of nodes to be used to approximate the value of the field function at any given point.
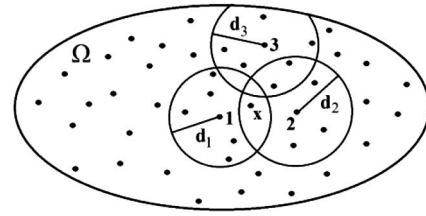
Fig. 4. Circular influence domains for nodes 1, 2, and 3 with radius of d_1, d_2, and d_3, respectively.

1. MLS Approximation

The meshless shape functions are constructed based on the MLS strategy and obtained by

$$u^b(\mathbf{x}) = \sum_{j}^{m} P_j(\mathbf{x}) a_j(\mathbf{x}) = \mathbf{P}^T(\mathbf{x}) \mathbf{a}(\mathbf{x}), \qquad (5)$$

where $\mathbf{P}^T(\mathbf{x})$ is a linear polynomial basis of order m and $\mathbf{a}(\mathbf{x})$ is a vector of coefficients to be determined.

The polynomial basis consists most often of monomials of the lowest orders to ensure minimum completeness:

$$\mathbf{P}^T(\mathbf{x}) = \{1, x, y, xy, x^2, y^2, \ldots, x^m, y^m\}. \qquad (6)$$

The unknown coefficients $\mathbf{a}(\mathbf{x})$ are obtained by minimizing the difference between the local approximation and the function, through

$$J = \sum_{i}^{n} w(\mathbf{x} - \mathbf{x}_i)[\mathbf{P}^T(\mathbf{x}_i)\mathbf{a}(\mathbf{x}) - u_i]^2, \qquad (7)$$

where $w(\mathbf{x} - \mathbf{x}_i)$ is the weight function with compact support (i.e., exactly zero outside a confinement radius), and n is the number of points in the neighborhood of $\mathbf{x}$ for which $w(\mathbf{x} - \mathbf{x}_i) \neq 0$.

The choice of the weight function is more or less arbitrary, as long as the function is positive and continuous. The most commonly used weight functions are the exponential, cubic spline, and quartic spline.

Exponential weight function [26]:

$$w(r) = \begin{cases} e^{-(r/0.4)^2}, & r \leq 1 \\ 0, & r > 1 \end{cases}. \qquad (8)$$

The weight function depends on r, where

$$r = \frac{\|\mathbf{x} - \mathbf{x}_i\|}{dm_i}. \qquad (9)$$

For a point of interest at $\mathbf{x}$, the dimension of the influence domain, dm_i, is determined by

$$dm_i = \alpha_s \cdot d_i, \qquad (10)$$

where d_i is the radius of the domain that defines the minimum number of nodes used for the approximation, and α_s is a scaling parameter. Generally, values of $\alpha_s = 2.0$ to 4.0 are used for static analysis [21–23].

The functional J can be minimized by setting its derivative with respect to $\mathbf{a}(\mathbf{x})$ equal to zero. It results in the following linear system:

$$\mathbf{A}(\mathbf{x})\mathbf{a}(\mathbf{x}) = \mathbf{B}(\mathbf{x})\mathbf{U}, \qquad (11)$$

where the matrices A and B are defined by

$$\mathbf{A}(\mathbf{x}) = \sum_{i=1}^{n} w(\mathbf{x} - \mathbf{x}_i)\mathbf{P}(\mathbf{x}_i)\mathbf{P}^T(\mathbf{x}_i), \qquad (12)$$

$$\mathbf{B}(\mathbf{x}) = [w(\mathbf{x} - \mathbf{x}_1)\mathbf{P}^T(\mathbf{x}_1) w(\mathbf{x} - \mathbf{x}_2)\mathbf{P}^T(\mathbf{x}_2)...w(\mathbf{x} - \mathbf{x}_n)\mathbf{P}^T(\mathbf{x}_n)], \qquad (13)$$

and the vector **U** contains all the nodal displacements:

$$\mathbf{U} = \sum_{i}^{n} u_i. \qquad (14)$$

The solution of the linear system from Eq. (10) is

$$\mathbf{a}(\mathbf{x}) = \mathbf{A}^{-1}(\mathbf{x})\mathbf{B}(\mathbf{x})\mathbf{U}. \qquad (15)$$

Note that the matrix **A** is always regular, i.e., invertible. Equation (12) shows that the minimum number of nodes depends on the polynomial basis function used.

Substituting Eq. (15) into Eq. (5), the MLS approximation is obtained:

$$u^h(\mathbf{x}) = \sum_{i}^{n} \sum_{j}^{m} p_j(\mathbf{x})[\mathbf{A}^{-1}(\mathbf{x})\mathbf{B}(\mathbf{x})]_{ji} u_i, \qquad (16)$$

where comparing with Eq. (4), the shape function ϕ_i associated with the node $\mathbf{x}_i$ is defined by

$$\phi_i(\mathbf{x}) = \sum_{j}^{m} p_j(\mathbf{x})(\mathbf{A}^{-1}(\mathbf{x})\mathbf{B}(\mathbf{x}))_{ji}. \qquad (17)$$

This can be written shortly as

$$\phi_i = \mathbf{P}^T \mathbf{A}^{-1} \mathbf{B}_i. \qquad (18)$$

Nevertheless, Eq. (4) also can be used for the displacement component $v(\mathbf{x})$, i.e.,

$$v(\mathbf{x}) = \sum_{i}^{n} \phi_i(\mathbf{x}) v_i. \qquad (19)$$

Using Eqs. (4) and (19), the displacement field in the deformed surface is defined as

$$\begin{Bmatrix} u \\ v \end{Bmatrix}^h = \sum_{i}^{n} \begin{bmatrix} \phi_i & 0 \\ 0 & \phi_i \end{bmatrix} \begin{Bmatrix} u_i \\ v_i \end{Bmatrix}. \qquad (20)$$

The strains are then computed using the strain-displacement relation given by

$$\begin{Bmatrix} \varepsilon_x \\ \varepsilon_y \\ \varepsilon_{xy} \end{Bmatrix}^h = \sum_{i}^{n} \begin{bmatrix} \frac{\delta}{\delta x} & 0 \\ 0 & \frac{\delta}{\delta y} \\ \frac{\delta}{\delta y} & \frac{\delta}{\delta x} \end{bmatrix} \begin{Bmatrix} u \\ v \end{Bmatrix}^h. \qquad (21)$$

Thus, in order to obtain strains from the displacement field, the partial derivatives of the MLS shape function are required, which can be obtained from Eq. (18) as

$$\phi_{i,x} = \mathbf{P}^T_{,x}\mathbf{A}^{-1}\mathbf{B}_i + \mathbf{P}^T(\mathbf{A}^{-1})_{,x}\mathbf{B}_i + \mathbf{P}^T\mathbf{A}^{-1}\mathbf{B}_{i,x}, \qquad (22)$$

$$\phi_{i,y} = \mathbf{P}^T_{,y}\mathbf{A}^{-1}\mathbf{B}_i + \mathbf{P}^T(\mathbf{A}^{-1})_{,y}\mathbf{B}_i + \mathbf{P}^T\mathbf{A}^{-1}\mathbf{B}_{i,y}, \qquad (23)$$

where the subscript represents the spatial derivation in the Cartesian coordinates frame.

Finally, using Eqs. (22) and (23), the expressions for the strain components can be obtained:

$$\begin{Bmatrix} \varepsilon_x \\ \varepsilon_y \\ \varepsilon_{xy} \end{Bmatrix}^h = \sum_{i}^{n} \begin{bmatrix} \phi_{i,x} & 0 \\ 0 & \phi_{i,y} \\ \phi_{i,x} & \phi_{i,y} \end{bmatrix} \begin{Bmatrix} u_i \\ v_i \end{Bmatrix}. \qquad (24)$$

2. Variable Domain of Influence

In the MLS approximation, a suitable influence domain is required to make a stable and accurate solution. The dimension of the influence domain, defined in Eq. (10), depends on two parameters: the radius of the influence domain d_i and the scaling parameter α_s.

The parameter d_i is determined by searching for enough nodes for the matrix A in Eq. (12) to be regular. In order to prevent the singularity of the matrix A, the number of nodes in the influence domain should be kept larger than the order of polynomial basis used for approximations, i.e., $n > m$. In this study, because of the high density of SIFT points extracted from the images, the minimum number of nodes is set to be much larger than the minimum requirements (with neighborhoods not less than 100 nodes).

The parameter α_s is a multiplier support that controls the actual dimension of the domain. The dimensionless size of α_s should be predetermined by the analyst. According to experimental results conducted by the authors, a $\alpha_s = 2.0$ through 4.0 lead to good results.

As an example, the results of preliminary testing conducted on laboratory are shown below using a notched specimen under bending load in the negative z direction. First, two images are
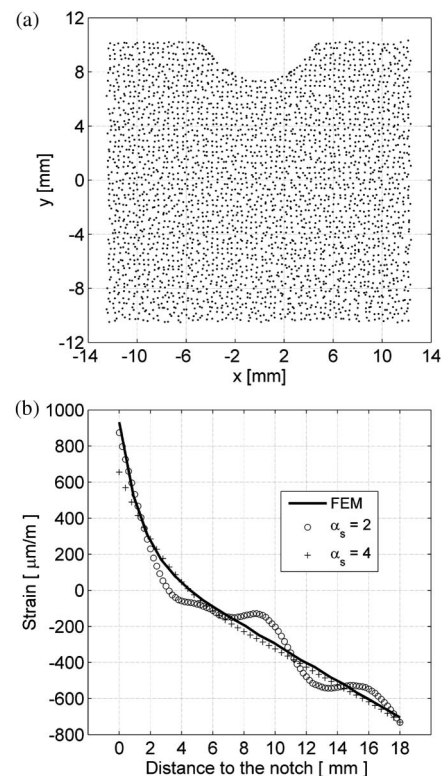
Fig. 5. (a) Nodes used to represent the problem domain. (b) Strain distributions for $\alpha_s = 2$ and $\alpha_s = 4$, and FEM result.
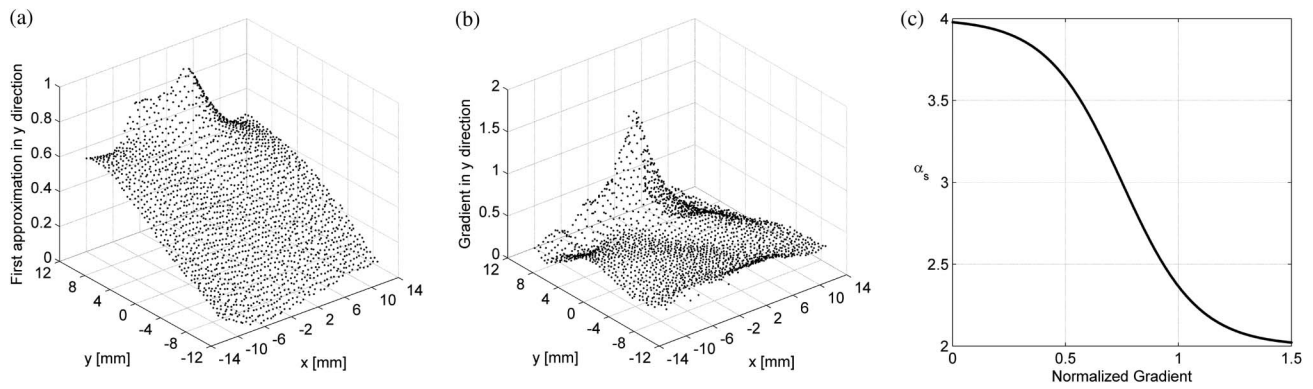
Fig. 6.　(a) First meshless approximation with $\alpha_s = 4$. (b) Magnitude of the gradient in y direction. (c) Test function to calculate the values of the α_s.

captured from testing, before and after the loading, and then processed by SIFT algorithm. Figure 5(a) shows a set of SIFT points successfully matched in a region around the notch. The strain components are calculated using meshless approximation described in Section 2.B. The strain distributions for the component ε_{xx} along the y axis at position $x = 0$ (notch root) with α_s values of 2 and 4 are plotted in Fig. 5(b) and compared with finite element method (FEM) simulation results. It is found that, when the influence domain is too small ($\alpha_s < 2.0$), not enough nodes have been used to perform an accurate approximation. If the influence domain is too large ($\alpha_s > 4.0$), the constructed shape functions become too smooth to correctly represent the singularities of the field variables.

Thus, in this study, the size of influence domain is set to be variable. The aim of this variability is to obtain more accurate results by decreasing the supporting nodes for approximation in areas with high stress concentration in which higher accuracy is required. On the other hand, the number of nodes increases in areas where the stress distribution is uniform; thus, a smoothed solution is provided.

For this purpose, a methodology is proposed here to automatically determine the values of α_s for each supported node: first, a meshless approximation is computed with a high value of α_s, which can be fixed at 4.0. This result is shown in Fig. 6(a). Then, the gradient of this first approximation in the direction of the notch is computed, as shown in Fig. 6(b). The magnitude of the gradient will show how fast the strain rises in that direction, indicating areas of high strain concentration.
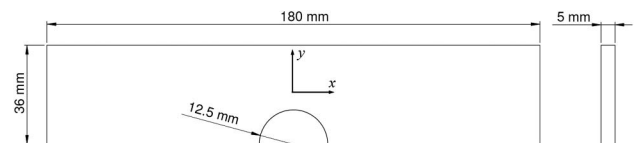
This information is useful for choosing a suitable value of α_s at each evaluation point, using for this purpose a test function similar to that shown in Fig. 6(c). This test function was constructed by means of numerical simulations of problems with stress concentration using Ansys software, whose solutions were known beforehand. Thereafter, with the new optimized values of α_s, the approximations are recomputed, and, finally, the strain distribution on the surface is obtained.
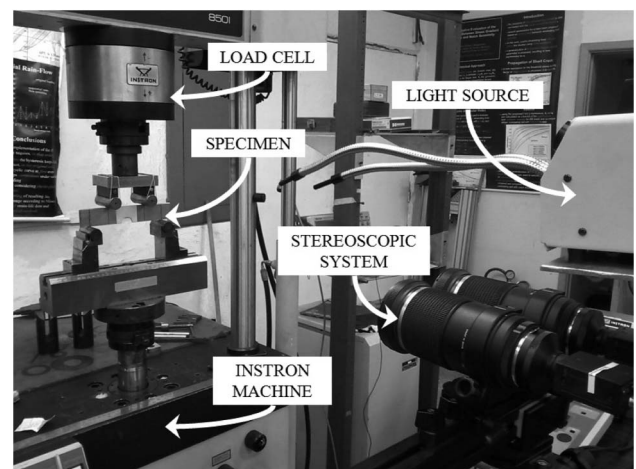
3. EXPERIMENTAL PROCEDURE

The proposed SIFT-meshless method is used to characterize and quantify the strain map around the notch root region of a 304 stainless-steel plate with a semicircular notch. For that,

the specimen is tested in a four-point bending configuration. The specimen geometry and dimensions are shown schematically in Fig. 7, where the y axis is the loading axis. To prepare the test specimen used here, a random black and white pattern was applied using spray paint, as described in Section 2.A.
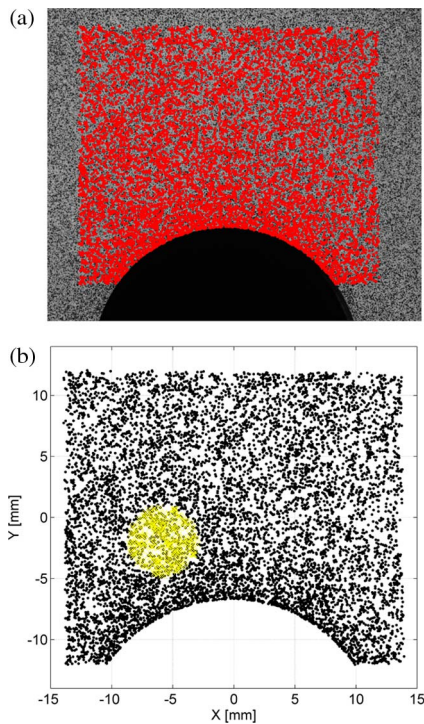
The mechanical test is performed in a servo-hydraulic Instron machine equipped with a four-point bend fixture. The inner and outer spans are fixed at 80 mm and 160 mm, respectively. For image acquisition, two charged-coupled device (CCD) cameras were placed in front of the specimen in a stereo configuration, as shown in Fig. 8. The used CCDs have a resolution of 2448×2048 pixels. The optical configuration results in a field of view of about 38 mm × 25 mm, with a pixel resolution of approximately 15.5 µm on the object plane. A fiber-optic

Fig. 7.　Notched steel specimen geometry.

Fig. 8.　Experimental arrangement.

Fig. 9. (a) SIFT features successfully matched within a region of interest plotted in the reference image. (b) Circular neighborhood represents the used influence domain for specific supported node.

Table 1. Number of Matches Returned by SIFT Technique

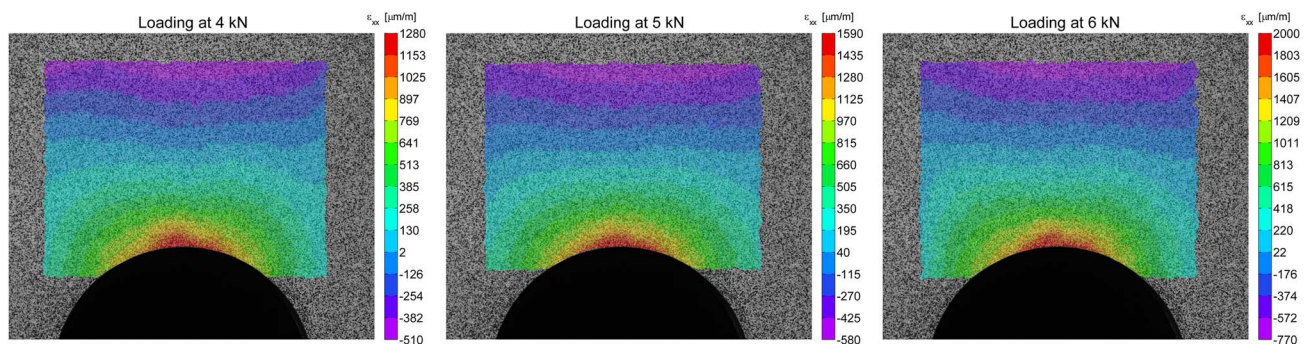| Load	SIFT Points Reference Image	SIFT Points Deformed Image	No. Matches
4 kN	16720	16599	9070
5 kN	16720	16687	8701
6 kN	16720	16563	8686

images. Table 1 contains details about the processing for each captured image while using the SIFT technique.

After the images have been processed, the meshless formulation is applied. For that, a quadratic basis function of six terms and the exponential weight function from Eq. (8) are used. The shape of the influence domain is circular with a minimum radius of 2.5 mm, about approximately 300 neighbor nodes, as shown in Fig. 9(b).

Therefore, the strain fields in the x direction for each load condition are computed (see Fig. 10). It can be seen that the effects of stress concentration are clearly identified in the specimen, where the maximum strain occurs at the bottom of the semicircular notch. The positive value is due to the bending moment applied to the specimen, which produces tensile stresses at the bottom of the beam and compressive stresses at the top.

The commercial VIC-3D software package from Correlated Solutions is applied to analyze the same acquired images. In DIC analysis, two parameters have to be set manually: the subset size and the step size. The subset size controls the area of the image that is used to track the displacement between images. The step size controls the spacing of the points that are analyzed during correlation. In this analysis, two subset sizes were tested with 21 and 41 pixels, corresponding to about 326 μm and 636 μm, respectively, on the object plane. The step size was set to 11 pixels for both analyses. Results using a subset size of 21 pixels are shown in Fig. 11.

Moreover, to check the consistency of the results, a 3D finite element analysis is performed using the ANSYS software. For that, the material properties and specimen dimensions are used as input data in the FE model. The mesh was created using tetrahedral elements and refined in the region around the notch for more accurate results. The 3D FE model for strain analysis is conducted under the same load conditions as the tested specimen.

illuminator is used to obtain a uniform illumination of the region of interest.

The cameras are calibrated before starting the test. The reference image is captured with the specimen in an unloaded state. Thereafter, successive load values of 4, 5, and 6 kN are applied to the bending specimen. For each increment of force, its corresponding image is captured, called "deformed image."

4. ANALYSIS AND RESULTS

Before the analysis, a region of interest is defined in the reference image. SIFT features are extracted from this region and then matched within the stereo-pair and within the consecutive images captured during the test. Figure 9(a) shows the features correctly matched for a given pair of reference/deformed
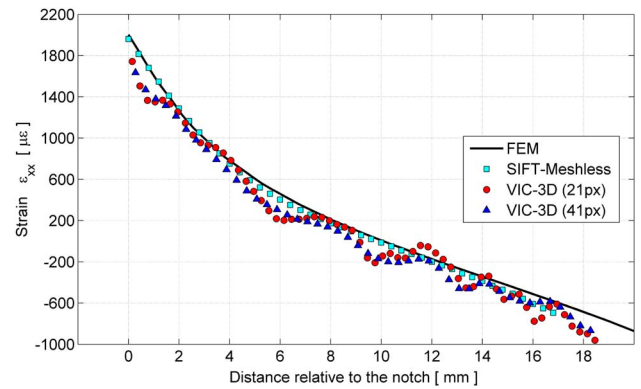

Fig. 10. Computed strain field in x direction measured by SIFT-meshless method for different values of loading.
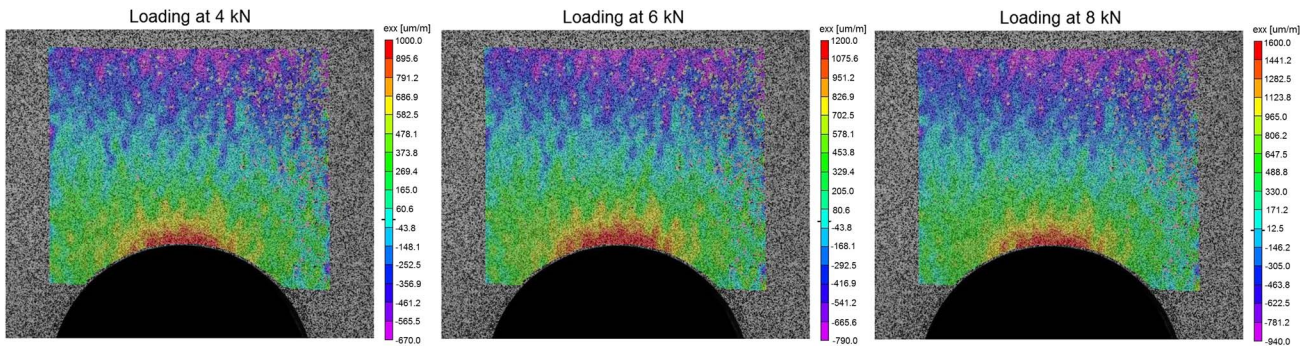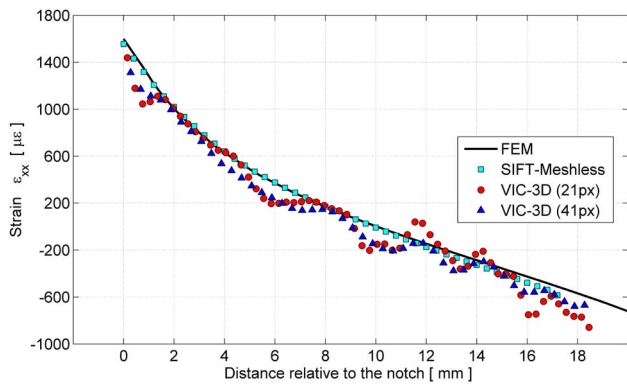
Fig. 11. Computed strain field in x direction measured by VIC-3D (subset = 21 pixels) for different values of loading.
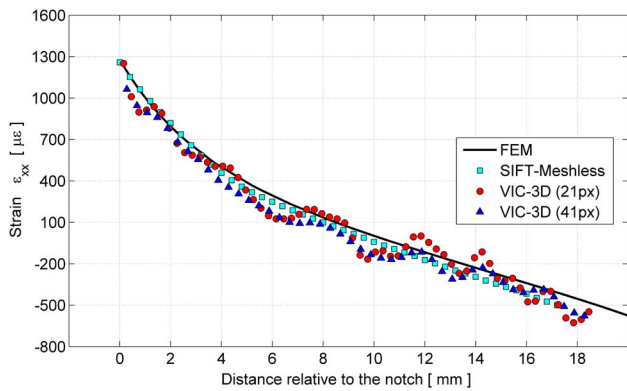
Fig. 12. Axial strains ε_{xx} on the y axis of the net section at 4 kN.

Fig. 14. Axial strains ε_{xx} on the y axis of the net section at 6 kN.

Fig. 13. Axial strains ε_{xx} on the y axis of the net section at 5 kN.

The results obtained by VIC-3D, SIFT-meshless, and ANSYS are then compared and analyzed. Figures 12 through 14 show the strain evolution along the net section in the vicinity of the notch ($x = 0$). Table 2 shows the maximum strain values obtained from the analysis.

Moreover, as shown in Figs. 12 through 14, the experimental and numerical results have the same trend. Good agreement is found between the responses measured by the proposed method and those predicted by the FE model. For the analysis using the VIC-3D software, the two solutions (with 21 and

41 pixels) are globally the same; however, the measured values are noisier with the smaller subset used. Moreover, the VIC-3D software can only capture strains from a finite distance of the notch surface. The nearest point of measurement using a subset size of 21×21 pixels ends up located at about 155 μm from the notch surface, significantly missing the peak strain in notches with high strain gradients. In addition, this small subset size clearly affects the smoothness of the strain distribution far from the notch. The increase of the subset size to 41×41 pixels reduces the waviness aspect of the response; however, the location of the nearest point of measurement is increased up to about 290 μm from the notch edge, degrading even further the identification of the peak strains from the notch tip.

These problems are solved by the proposed SIFT-meshless method. Use of the SIFT technique allows extracting displacement measurements at the notch tip, since features are detected in this region and not beginning at some finite distance beyond its surface. Moreover, the meshless formulation with variable influence domain adapts the calculations to the presence of low- and high-strain gradients in the same analyzed region and improves accuracy in the measurement results around the notch tip.

Last, Table 3 shows the results of the analysis of uncertainty for the SIFT-meshless method. For that, two images of the specimen taken in the unloaded stage are analyzed, which, in theory, are equal.

Table 2.   Maximum Strain at Notch Root Obtained by FE, SIFT-Meshless, and VIC-3D

Analysis	Distance from Notch Edge [mm]	Maximum Strain (με)		
		4 kN	5 kN	6 kN
FEM	0	1279	1599	2002
SIFT-Meshless	0	1258	1556	1960
VIC-3D (21 px)	0.15	1334	1423	1766
VIC-3D (41 px)	0.29	1063	1311	1635

Table 3.   Uncertainty Analysis of the SIFT-Meshless Method

Component	RMS Error	Max. RMS Error
$u(x, y)$	3.5 μm	3.8 μm
$\varepsilon_{xx}(x, y)$	24 με	96 με

The errors shown in Table 3 are intrinsic to the image spatial resolution, camera calibration, the texture applied to the material, and errors related to SIFT algorithm. Therefore, they must not increase significantly with the applied load.

5. CONCLUSIONS

In the present work, a novel hybrid technique is introduced for full-field strain measurements and its application to the analysis of the deformation behavior in regions of stress concentration. During the development of the methodology, advanced computer vision techniques have been incorporated, such as the SIFT technique in combination with spatial reconstruction and stereoscopic vision systems. The main contribution of this work is the fusion of these techniques with meshless methods, thereby greatly improving the accuracy for strain measurements, in particular, around notches or any other stress concentrator, where the maximum strains are located.

The SIFT descriptors demonstrated its capability to offer robust and stable image matching results for measuring displacement on the surface of the specimen. Furthermore, the use of SIFT points as nodes in the meshless formulation has been applied successfully for modeling the displacements and the corresponding strain field. The meshless formulation proposed here allows direct connection between the SIFT features and numerical calculations.

The experimental strain data measured by the SIFT-meshless method in a 304 stainless-steel plate with a semicircular notch are in agreement with the finite element predictions. In comparison with DIC techniques, the SIFT-meshless method obtained more accurate measurements in the region immediately ahead of the notch, where errors of larger magnitude are expected, since these high-gradient regions are sensitive to DIC parameters chosen for the analysis. The results indicate that the proposed methodology can be a useful tool for measuring strain fields around sharper notches and even cracks, increasing its applicability in experimental mechanics.

REFERENCES

1. J. E. Shigley, *Shigley's Mechanical Engineering Design* (McGraw-Hill, 2011).
2. N. T. Younis and B. Kang, "Averaging effects of a strain gage," J. Mech. Sci. Tech. **25**, 163–169 (2011).
3. T. Chu, W. Ranson, and M. Sutton, "Applications of digital-image-correlation techniques to experimental mechanics," Exp. Mech. **25**, 232–244 (1985).
4. M. Sutton, W. Wolters, W. Peters, W. Ranson, and S. McNeill, "Determination of displacements using an improved digital correlation method," Image Vis. Comput. **1**, 133–139 (1983).
5. H. Bruck, S. McNeill, M. A. Sutton, and W. Peters III, "Digital image correlation using Newton-Raphson method of partial differential correction," Exp. Mech. **29**, 261–267 (1989).
6. M. A. Sutton, S. R. McNeill, J. D. Helm, and Y. J. Chao, "Advances in two-dimensional and three-dimensional computer vision," in *Photomechanics* (Springer, 2000), pp. 323–372.
7. J. Gao and H. Shang, "Deformation-pattern-based digital image correlation method and its application to residual stress measurement," Appl. Opt. **48**, 1371–1381 (2009).
8. B. Pan, D. Wu, and L. Yu, "Optimization of a three-dimensional digital image correlation system for deformation measurements in extreme environments," Appl. Opt. **51**, 4409–4419 (2012).
9. Z. Tang, J. Liang, Z. Xiao, and C. Guo, "Large deformation measurement scheme for 3D digital image correlation method," Opt. Lasers Eng. **50**, 122–130 (2012).
10. F. Lagattu, J. Brillaud, and M.-C. Lafarie-Frenot, "High strain gradient measurements by using digital image correlation technique," Mater. Charact. **53**, 17–28 (2004).
11. C. Qian, L. Harper, T. Turner, and N. Warrior, "Notched behaviour of discontinuous carbon fibre composites: comparison with quasi-isotropic non-crimp fabric," Compos. Part A **42**, 293–302 (2011).
12. S.-F. Hwang and W.-J. Wu, "Deformation measurement around a high strain-gradient region using a digital image correlation method," J. Mech. Sci. Tech. **26**, 3169–3175 (2012).
13. B. Pan, H. Xie, Z. Wang, K. Qian, and Z. Wang, "Study on subset size selection in digital image correlation for speckle patterns," Opt. Express **16**, 7037–7048 (2008).
14. M. A. Sutton, J.-J. Orteu, and H. W. Schreier, *Image Correlation for Shape, Motion and Deformation Measurements* (Springer, 2009).
15. D. G. Lowe, "Object recognition from local scale-invariant features," in *Proceedings of the Seventh IEEE International Conference on Computer Vision* (IEEE, 1999).
16. D. G. Lowe, "Distinctive image features from scale-invariant keypoints," Int. J. Comput. Vis. **60**, 91–110 (2004).
17. K. Mikolajczyk and C. Schmid, "A performance evaluation of local descriptors," IEEE Trans. Pattern Anal. Mach. Intell. **27**, 1615–1630 (2005).
18. F. Remondino, "Detectors and descriptors for photogrammetric applications," Int. Arch. Photogramm. Remote Sens. Spatial Inf. Sci. **36**, 49–54 (2006).
19. G.-R. Liu and Y.-T. Gu, *An Introduction to Meshfree Methods and Their Programming* (Springer, 2005).
20. V. P. Nguyen, T. Rabczuk, S. Bordas, and M. Duflot, "Meshless methods: a review and computer implementation aspects," Math. Comput. Simulation **79**, 763–813 (2008).
21. G.-R. Liu, *Meshfree Methods: Moving Beyond The Finite Element Method* (CRC Press, 2010).
22. T. Belytschko, Y. Y. Lu, and L. Gu, "Element-free Galerkin methods," Int. J. Numer. Methods Eng. **37**, 229–256 (1994).
23. J. Dolbow and T. Belytschko, "An introduction to programming the meshless element free Galerkin method," Arch. Comput. Methods Eng. **5**, 207–241 (1998).
24. C. Solutions, http://www.correlatedsolutions.com.
25. D. Lowe, "Demo software: SIFT keypoint detector, 2008," Demo available for download at http://www.cs.ubc.ca/~lowe/keypoints (2011).
26. T. Belytschko, D. Organ, and Y. Krongauz, "A coupled finite element-element-free Galerkin method," Comput. Mech. **17**, 186–195 (1995).